

# Simulation Model of Reactive Nitrogen Species in an Urban Atmosphere using a Deep Neural Network: RNDv1.0

Junsu Gil<sup>1</sup>, Meehye Lee<sup>1\*</sup>, Jeonghwan Kim<sup>2</sup>, Gangwoong Lee<sup>2</sup>, Joonyoung Ahn<sup>3</sup>

<sup>1</sup> Department of Earth and Environmental Science, Korea University, Seoul, South Korea

<sup>2</sup> Department of Environmental Science, Hankuk University of Foreign Studies, Yongin, South Korea

<sup>3</sup> Air Quality Forecasting Center, Climate and Air Quality Research Department, National Institute of Environmental Research (NIER), Incheon, South Korea

\* Corresponding author: Meehye Lee ([meehye@korea.ac.kr](mailto:meehye@korea.ac.kr))

## Abstract

Nitrous acid (HONO), one of the reactive nitrogen oxides (NO<sub>y</sub>), plays an important role in the formation of ozone (O<sub>3</sub>) and fine aerosols (PM<sub>2.5</sub>) in the urban atmosphere. In this study, a new simulation approach to calculate HONO mixing ratios using a deep neural technique based on measured variables was developed. The 'Reactive Nitrogen species simulation using Deep neural network' (RND) has been implemented in Python. It was trained, validated, and tested with HONO measurement data obtained in Seoul during the warm months from 2016 to 2019.

A k-fold cross validation and test results confirmed the performance of RND v1.0 with an Index Of Agreement (IOA) of 0.79 ~ 0.89 and a Mean Absolute Error (MAE) of 0.21 ~ 0.31 ppbv. The RNDV1.0 adequately represents the main characteristics of HONO and thus, RND v1.0 is proposed as a supplementary model for calculating the HONO mixing ratio in a high-NO<sub>x</sub> environment.

## 1. Introduction

30

31 Surface ozone (O<sub>3</sub>) pollution has been reported to be worsen over continental areas  
32 (Arnell et al., 2019;Monks et al., 2015;Varotsos et al., 2013;IPCC, 2014). In particular, a  
33 warmer climate is expected to increase surface O<sub>3</sub> and intensity of surface O<sub>3</sub> peaks in polluted  
34 regions, depending on its precursor levels (IPCC 2021). As one of the short-lived climate  
35 pollutants (SLCPs), O<sub>3</sub> also interacts with the global temperature via positive feedback  
36 (Shindell et al., 2013;Myhre et al., 2017;Stevenson et al., 2013). Therefore, it is imperative to  
37 accurately predict the mixing ratios and variations of surface O<sub>3</sub>. While operational models such  
38 as community multiscale air quality (CMAQ) have been used widely for this purpose,  
39 uncertainties still arise from poorly understood chemical mechanisms involving reactive  
40 nitrogen oxides (NO<sub>y</sub>) and volatile organic compounds (VOCs), and lack of their measurements  
41 (Mallet and Sportisse, 2006;Canty et al., 2015;Akimoto et al., 2019;Shareef et al., 2019;Cheng  
42 et al., 2022).

43 In the urban atmosphere, NO<sub>y</sub> typically includes NO<sub>x</sub> (NO + NO<sub>2</sub>), HONO, HNO<sub>3</sub>,  
44 organic nitrates (e.g., PAN), NO<sub>3</sub>, N<sub>2</sub>O<sub>3</sub>, and particulate NO<sub>3</sub><sup>-</sup>. These species are produced and  
45 recycled through photochemical reactions until they are removed through wet or dry deposition  
46 (Liebmann et al., 2018;Brown et al., 2017;Wang et al., 2020;Li et al., 2020). NO<sub>y</sub> play an  
47 important role in critical environmental issues concerning the Earth's atmosphere, spanning  
48 from local air pollution to global climate change (Sun et al., 2011;Ge et al., 2019). The oxidation  
49 of NO to NO<sub>2</sub>, and finally to HNO<sub>3</sub>, is the backbone of the chemical mechanism producing  
50 ozone (O<sub>3</sub>) and PM<sub>2.5</sub> (particulate matter of size  $\leq 2.5 \mu\text{m}$ ), and it determines the oxidization  
51 capacity of the atmosphere. Recently, as O<sub>3</sub> has increased along with a decrease in NO<sub>x</sub> emission  
52 over many regions including East Asia, interest in the heterogeneous reaction of reactive  
53 nitrogen oxides, which is yet to be understood, has been newly raised (Brown et al.,  
54 2017;Stadtler et al., 2018). Currently, the lack of measurement of individual NO<sub>y</sub> species  
55 hindered a comprehensive understanding of the heterogeneous reactions (Anderson et al.,  
56 2014;Wang et al., 2017b;Chen et al., 2018b;Akimoto and Tanimoto, 2021;Stadtler et al., 2018).

57 In particular, there are growing number of evidence for heterogeneous formation of  
58 HONO in relation to high PM<sub>2.5</sub> and O<sub>3</sub> occurrence in urban areas (e.g., (Li et al., 2021b)). As  
59 an OH reservoir, HONO will expedite the photochemical reactions involving VOCs and NO<sub>x</sub>  
60 in the early morning, leading to O<sub>3</sub> and fine aerosol formation. Nonetheless, its formation

61 mechanism has not been elucidated clearly enough to be constrained in conventional  
62 photochemical models. In addition to the reaction of NO with OH (Bloss et al., 2021), various  
63 pathways of HONO formation have been suggested from laboratory experiments, field  
64 measurements and model simulations: direct emissions from vehicles (e.g., (Li et al., 2021a))  
65 and soil (e.g.,(Bao et al., 2022)), photolysis of particulate nitrate (e.g., (Gen et al., 2022)), and  
66 heterogeneous conversion of NO<sub>2</sub> on various aerosol surfaces (e.g., (Jia et al., 2020)), ground  
67 surface (e.g.,(Meng et al., 2022)), and microlayers of sea surface (e.g., (Gu et al., 2022)).  
68 Among these, heterogeneous reaction mechanism at surface is major concern in recently HONO  
69 study.

70 HONO has been measured mostly during intensive campaigns in urban areas using  
71 various techniques such as a long path absorption photometer (LOPAP) (Kleffmann et al.,  
72 2006;Xue et al., 2019), chemical ionization mass spectrometry (CIMS) (Levy et al.,  
73 2014;Roberts et al., 2010), ion chromatography (IC) (VandenBoer et al., 2014;Gil et al.,  
74 2020;Ye et al., 2016;Xu et al., 2019), and quantum cascade tunable infrared laser differential  
75 absorption spectrometry (QC-TILDAS) (Lee et al., 2011;Gil et al., 2021). Of these methods,  
76 QC-TILDAS has served as a reference for intercomparison of measurement data from different  
77 techniques due to high time resolution and stability (Pinto et al., 2014). These studies reported  
78 the maximum HONO of several ppb levels at nighttime. In comparison, the model captured at  
79 most 67~90 % of the observed HONO in megacities such as Beijing (Tie et al., 2013;Liu et al.,  
80 2019).

81 In recent years, Machine Learning (ML) method has been adopted in the atmospheric  
82 science for pattern classification (e.g. New Particle Formation event) and forecasting and  
83 spatiotemporal modelling of O<sub>3</sub> and PM<sub>2.5</sub> (Arcomano et al., 2021;Shahriar et al.,  
84 2020;Krishnamurthy et al., 2021;Cui and Wang, 2021;Joutsensaari et al., 2018;Chen et al.,  
85 2018a;Kang et al., 2021). Among ML methods, the Neural Network (NN) architecture is widely  
86 used owing to its powerful ability to process large amounts of data, allowing improvement in  
87 the performance of conventional models through being integrated with physical equations  
88 (Reichstein et al., 2019;Schultz et al., 2021). As a NN architecture, a multi-layer artificial neural  
89 network, referred to as a Deep Neural Network (DNN), employs a statistical method that learn  
90 non-linear relations in data and obtain the optimum solution for the target species without prior  
91 information on the physicochemical processes. DNN has advantages over other NN architecture

92 such as Convolution NN (CNN) or Long-Short Term Memory (LSTM) because it works well  
93 for discrete spatiotemporal data. In general, the performance of DNN is similar to or better than  
94 other ML methods for small number of data as well as large data set (Baek and Jung, 2021; Dang  
95 et al., 2021; Sumathi and Pugalendhi, 2021).

96 When the DNN method is applied to atmospheric chemical constituents, it requires  
97 large amount of data for training and thus, the size of measurement data becomes a limiting  
98 factor for trace species such as HONO, which are not routinely measured such as O<sub>3</sub> or PM<sub>2.5</sub>.  
99 In this regard, the daily average HONO mixing ratio was attempted to be estimated using  
100 ensemble ML models with satellite measurements (Cui and Wang, 2021). In comparison, the  
101 hourly HONO mixing ratio was calculated using a simple NN architecture with measured  
102 variables, which were thought to be closely linked with HONO formation (Gil et al., 2021). The  
103 accuracy of the hourly HONO estimated from input variables such as aerosol surface areas and  
104 mixed layer height was better than the daily HONO estimate.

105 In this study, we aimed to construct a user-friendly ‘Reactive Nitrogen species  
106 simulation using DNN’ (RND) model and estimate HONO mixing ratio using routinely  
107 measured atmospheric variables in a highly polluted urban area. Finally, the model results will  
108 be incorporated into operational photochemical models for air quality forecasting and improve  
109 their performance. Since this is the first attempt to calculate HONO mixing ratios using a first  
110 version of RND model (RNDv1.0), we describe the entire modeling process and evaluate the  
111 model results by comparing them with the measurements.

112

## 113 **2. Model description**

114

115 The development of RNDv1.0 model follows the systematic steps similar to a general  
116 machine learning model construction workflow, including collecting data, preprocessing data,  
117 building the DNN, training and validating the model, and testing the performance of the model  
118 (Figure 1). The RNDv1.0 was written in Python and necessary libraries to build and operate  
119 RNDv1.0 are listed in Table 1. The dataset used to train-test-validation can be downloaded from  
120 Gil et al., 2021.

121

## 122 **2.1. Collection of measurement data for model construction**

123

124 As the first step constructing the RNDv1.0, measurement data were obtained including  
125 HONO, reactive gases, and meteorological parameters. **It is noteworthy that the HONO**  
126 **measurement data is for model construction and is not required to run the RND model.** The  
127 HONO mixing ratio was measured using a Quantum Cascade – Tunable Infrared Laser  
128 Differential Absorption Spectrometer (QC-TILDAS) system in Seoul during May–June 2016,  
129 June 2018, and April–June 2019 (Lee et al., 2011; Gil et al., 2021). When testing and evaluating  
130 atmospheric HONO measurement methods, QC-TILDAS has been chosen as the reference  
131 method for comparing ambient HONO mixing ratios measured using several different  
132 techniques owing to its advantages of low detection limits (~ 0.1 ppbv) and high temporal  
133 resolution (Pinto et al., 2014). More details on measurements can be found elsewhere (Gil et  
134 al., 2021). HONO was measured at Olympic Park (37.52°N, 127.12°E) during the Korea-United  
135 States Air Quality (KORUS-AQ) study in 2016 (Kim et al., 2020; Gil et al., 2021), at the campus  
136 of Korea University in 2018 (37.59°N, 127.03°E), and at the site near the campus in 2019  
137 (37.59°N, 127.08°E) (NIER, 2020) (Figure S1). Of the three sites, the Korea University campus  
138 and Olympic Park have served as measurement sites representing the air quality of Seoul. In  
139 fact, it has been known that O<sub>3</sub> and PM<sub>2.5</sub> levels are strongly influenced by the synoptic  
140 circulation throughout the Korean peninsula (Peterson et al., 2019; Jordan et al., 2020). In  
141 addition, trace gases including O<sub>3</sub>, NO<sub>2</sub>, CO, and SO<sub>2</sub> and meteorological parameters including  
142 temperature (T), relative humidity (RH), wind speed (WS) and direction (WD) were measured.  
143 **Note that HONO was not significantly correlated with any of these variables (Figure S2).** The  
144 measurement statistics are presented in Table 2 and Table S1. Briefly summarizing, the 10<sup>th</sup> and  
145 90<sup>th</sup> percentile mixing ratios of HONO, NO<sub>2</sub>, and O<sub>3</sub> are 0.3 ppbv and 1.9 ppbv, 10.7 ppbv and  
146 48.2 ppbv, and 12.0 ppbv and 80.9 ppbv, respectively for the entire experiment periods.

147

## 148 **2.2. Data preprocessing**

149

150 In the next step, the observation data set was prepared for RNDv1.0 model construction.  
151 As input variables, hourly measurements of chemical and meteorological parameters are used,  
152 including the mixing ratios of O<sub>3</sub>, NO<sub>2</sub>, CO, and SO<sub>2</sub>, along with temperature (T), relative  
153 humidity (RH), wind speed (WS), wind direction (WD), and solar zenith angle (SZA) to  
154 estimate the target species, HONO, as the output. Wind direction in degrees were converted to  
155 a cosine value for continuity. As a last step in data processing, missing values were filtered out  
156 from the input dataset. Finally, 50.7 % of all available measurement data (1636) were used to  
157 construct the RNDv1.0 in this study.

158 Since the measurements of these nine variables vary over a wide range in different units,  
159 they were normalized to avoid bias during the calculations. Among the widely used  
160 normalization methods, ‘*min-max scaling*’ method was adopted and input variables were  
161 normalized against the minimum and maximum values in this study (Eq. 1):

$$162 \quad x_{\text{sca}} = \frac{x_{\text{raw}} - F_2(X)}{F_1(X)}, \quad (1)$$

164 where  $x_{\text{raw}}$  is raw data of input variable (X),  $x_{\text{sca}}$  is scaled data of X,  $F_1$  and  $F_2$  are scale  
165 factors of X, and are given for each input variable used in Table 2.  
166

167

### 168 **2.3. Neural network architecture and hyperparameters**

169

170 At this stage, the network is built to calculate HONO using those input variables. The  
171 RNDv1.0 is composed of five hidden layers (Figure 2), which employed an exponential linear  
172 unit (ELU) as an activation function (Eq. 2).

173

$$174 \quad \text{ELU: } \phi(x) = \begin{cases} e^x - 1 & (x < 0) \\ x & (x \geq 0) \end{cases}. \quad (2)$$

175

176 In a DNN, an activation function creates a nonlinear relationship between an input  
 177 variable and an output variable. When constructing a DNN model, an ELU has the advantage  
 178 of a fast-training process and better performance in handling negative values than other  
 179 activation functions (Wang et al., 2017a;Ding et al., 2018). In addition, the mean squared error  
 180 and Adam optimizer were applied as loss function and optimize function, respectively. The  
 181 learning rate, epoch, and batch were set to 0.01, 100, and 32, respectively.

182

## 183 **2.4. Train, validation, and test**

184

185 The RNDv1.0 model was trained, validated, and tested with HONO measurements obtained  
 186 during May ~ June in 2016 and 2019, in June 2018, and in April 2019, respectively (Figure 3).  
 187 The number of data used for train, validation, and test were 1122, 381, and 133, respectively.

188 With the hyperparameters specified in previous section, the performance of the model was  
 189 firstly validated using the k-fold cross-validation method, which is especially useful when the  
 190 size of dataset is small (Bengio and Grandvalet, 2003). In the k-fold cross-validation method  
 191 (Figure 3), the entire data is randomly divided into k subsets, of which k-1 sets were used for  
 192 training and the rest one was used for validation. k was set to 5 in this study. The accuracy was  
 193 determined by Index Of Agreement (IOA) and Mean Absolute Error (MAE) expressed by the  
 194 following equation (Eq. 3, Eq. 4):

195

$$196 \quad IOA = 1 - \frac{\sum_{i=1}^n (O_i - P_i)^2}{\sum_{i=1}^n (|P_i - \bar{O}| + |O_i - \bar{O}|)^2}, \quad (3)$$

$$197 \quad MAE = \frac{\sum_{i=1}^n |O_i - P_i|}{n}, \quad (4)$$

198

199 where  $O_i$ ,  $P_i$ ,  $\bar{O}$ , and n are the observed value, predicted value, average of the observed  
 200 values, and number of nodes, respectively. The overall accuracy of

201 As IOA and MAE vary according to the number of nodes, they were calculated for the  
 202 measured (HONO<sub>obs</sub>) and calculated (HONO<sub>mod</sub>) mixing ratios by varying the number of nodes  
 203 from 0 to 100 in each hidden layer. The best performance was found with 41 nodes, with which

204 the averaged IOA and MAE were  $0.89 \pm 0.01$  (mean  $\pm$  standard deviation) and  $0.31 \pm 0.02$  ppbv,  
205 respectively (Figure 4). The high level of IOA and low MAE demonstrates that the performance  
206 of RNDv1.0 model is adequate, and it is capable of simulating the ambient HONO mixing ratio  
207 using the routinely measured chemical and meteorological parameters. In particular, MAE was  
208 commensurate with the detection limit of HONO measurement.

209 After the network validation, HONO mixing ratio was calculated for May ~ June in 2016  
210 and 2019, and the model results were compared with the measured values (Figure 5). The  
211 average mixing ratios of measured and calculated HONO was 0.94 ppbv and 0.89 ppbv in 2016,  
212 and 1.02 ppbv and 0.96 ppbv in 2019, respectively. The MAE and IOA of the measurement and  
213 calculation were 0.27 ppbv and 0.90 in 2016, and 0.29 ppbv and 0.91 in 2019, respectively,  
214 demonstrating the ability of the RNDv1.0 to simulate ambient HONO levels. In both cases,  
215 however, the model slightly underestimated the highest and lowest HONO mixing ratios, which  
216 is mainly due to the limited number of data used for training, but also related to the intrinsic  
217 nature of DNN. The model calculation well captured the diurnal variation of ambient HONO  
218 with a slight underestimation (Figure 6). In addition, the correlation between  $\text{HONO}_{\text{mod}}$  and  
219  $\text{HONO}_{\text{obs}}$  was better in 2019 (MAE = 0.06 ppbv) than in 2016 (MAE = 0.08 ppbv). Since the  
220 MAE of the two cases was far below the detection limit of HONO measurements ( $\sim 0.1$  ppbv),  
221 the RNDv1.0 is considered adequate to simulate HONO in urban areas.

222 Finally, the RND model was validated and tested against the measurement data obtained in  
223 June 2018 and April 2019. The calculated HONO mixing ratios are compared with those  
224 measured in Figure 7, and their MAE and IOA are listed in Table 3. The two sets of model  
225 performance test showed that the model reasonably traced what was observed. As the validation  
226 result of RND, the MAE and IOA of the calculated and measured in June 2018 are comparable  
227 to those of 2016~2019 result. However, the MAE and IOA of the April 2019 measurements  
228 were relatively poor compared to the validation results. Especially, the MAE of the April 2019  
229 is about twice as high as those of validation.

230 In these two test periods, HONO levels were lower than those observed on validation days  
231 (Figure 5), and the model tended to overestimate high HONO concentrations. The large  
232 discrepancy in April 2019 is probably due to seasonality: the difference in meteorological and  
233 chemical regime of the atmosphere. For example, the monthly average temperature, relative  
234 humidity, and  $\text{NO}_2$  mixing ratio of Seoul in 2019 were  $12.1$  °C, 50.9 %, and 29 ppbv in April



235 2019 and 22.5 °C, 60.6 %, and 21 ppbv in June 2019 (<https://cleanair.seoul.go.kr>;  
236 <https://weather.go.kr>). Note that the RNDv1.0 model was trained with the 9 variables measured  
237 in early summer (Table 2). Therefore, the more measurement data spanning a full year for  
238 training, the more accurate the model estimates will be.

239

## 240 **2.5. Influence of input variables to HONO concentration**

241

242 Additionally, a simple bootstrapping test was conducted by setting each variable to zero  
243 with keeping other variables (Kleinert et al., 2021). Then, the importance of each input variable  
244 to HONO concentration was evaluated using MAE and root mean square error (RMSE). Of  
245 nine input variables, NO<sub>2</sub> was found to have the most significant influence on HONO  
246 concentration, followed by RH, temperature, and solar zenith angle (Table S2). The result of  
247 bootstrap test is in good agreement with those from our previous study (Gil et al., 2021), where  
248 more detailed information such as aerosol surface area and mixing layer height were  
249 incorporated into the model and highlighted the role of precursor gases and heterogeneous  
250 conversion in HONO formation. Therefore, these results demonstrate that the RND model  
251 constructed using routinely observed variables, reasonably traced the level of HONO in urban  
252 atmosphere.

253

## 254 **3. Operation and application of RNDv1.0**

255

256 The RNDv1.0 package is provided as an operational model, .h5 files that can be opened in  
257 Python. To run the RNDv1.0, the measurement data for nine input variables are required and  
258 need to be properly prepared as described in Section 2.2. A sample of preprocessed input dataset  
259 is provided as a .csv file (Dataset\_for\_model.csv). Once the input data is ready, open the RND  
260 model with input data files using the code provided in the example (Figure S3). Then, RND  
261 v1.0 calculates and presents the HONO results as scaled values ( $x_{sca}$ ), which will be finally  
262 converted to HONO mixing ratio (ppbv) by the two scale factors in Table 2 (Eq. 5):

263

$$264 \quad \text{HONO (ppbv)} = \text{HONO}_{\text{sca}} \times F_1(\text{HONO}) + F_2(\text{HONO}). \quad (5)$$

265

266 The result of the RNDv1.0, HONO, can be applied to an urban photochemical cycle  
267 simulation. It is already known that the photolysis of HONO is a major source of OH radicals  
268 in the early morning when the OH level is low, and this OH affects daytime O<sub>3</sub> formation  
269 through photochemical reactions with VOCs and NO<sub>x</sub>, which are primarily emitted during  
270 morning rush hour in urban areas. Therefore, the OH produced from HONO expedites  
271 photochemical reactions, promoting O<sub>3</sub> formation. However, the HONO formation mechanism  
272 is still poorly understood, and concentrations are not correctly simulated in conventional  
273 photochemical models; therefore, the absence of HONO causes great uncertainty in O<sub>3</sub>  
274 prediction (Figure 8).

275 The 0-Dimension Atmospheric Modelling (F0AM) utilizing the MCM v3.3.1 chemical  
276 reaction mechanisms (Wolfe et al., 2016), can be used to simulate the diurnal variation of O<sub>3</sub>  
277 with the measurements of several reactive gases (NO, NO<sub>2</sub>, CO, HCHO, VOCs, and HONO).  
278 Detailed information about F0AM can be found in  
279 (<https://sites.google.com/site/wolfegm/models>) and in previous works published elsewhere  
280 (Wolfe et al., 2016; Gil et al., 2020). When the F0AM model is run without HONO, it is not  
281 able to reproduce the concentration and diel cycle of the observed O<sub>3</sub> (Figure 8). In comparison,  
282 the model simulates the O<sub>3</sub> well within 2 ppbv when adding HONO, which is the product of  
283 RND v1.0. This is mainly due to the missing OH produced by HONO photolysis in the early  
284 morning. Its production rate is estimated to be 0.57 pptv s<sup>-1</sup>, contributing approximately 2.28  
285 pptv to OH budget during 06:00 ~ 11:00 (LST) (Gil et al., 2021). Given that OH is mainly  
286 produced from the photolysis of O<sub>3</sub> under high sun, the early morning source of OH will  
287 expedite the photochemical cycle involving NO<sub>x</sub> and VOCs, promoting O<sub>3</sub> and secondary  
288 aerosol formation. Since the presence of HONO in the photochemical model allows for accurate  
289 estimation of OH radicals, the incorporation of RND into conventional models will improve  
290 their overall performance.

291

#### 292 **4. Summary and implications**

293

294 In this study, we developed the RND model to calculate the mixing ratio of  $\text{NO}_y$  in an urban  
295 atmosphere using a DNN along with measurement data. The target species of RNDv1.0 is  
296 HONO, and its mixing ratio is calculated using trace gases including  $\text{O}_3$ ,  $\text{NO}_2$ , CO, and  $\text{SO}_2$ ,  
297 and meteorological variables including T, RH, WS, and WD, along with the SZA. These  
298 variables are routinely measured through monitoring networks. The RNDv1.0 was trained and  
299 validated using the HONO measurements obtained in Seoul by adopting a k-fold cross  
300 validation method and tested with other HONO datasets measured using the same instrument.  
301 The validation and test results demonstrate that RND adequately captures the characteristic  
302 variation of HONO and confirms the efficacy of RND v1.0.

303 RNDv1.0 was constructed using measurements made in a high  $\text{NO}_x$  environment during  
304 early summer (May–June). It is noteworthy that in this period, the HONO mixing ratio was  
305 raised above 3 ppbv with the highest  $\text{O}_3$  levels under stagnant conditions. If RND is applied to  
306 areas under significant influence of outflows, the model possibly overestimates or  
307 underestimate the level of HONO without detailed information such as nanoparticles. In the  
308 previous study, the formation of HONO was shown to be intimately related with surface areas  
309 of submicron particles (Gil et al., 2021). [Nevertheless, the HONO concentration produced from  
310 RNDv1.0 with routine measurements provides the benefit of relatively inexpensive test for  
311 measurement quality control, location selection, and supports the data used for traditional  
312 chemistry model based on the current knowledge of the urban photochemical cycle.](#) Therefore,  
313 it is reasonable to argue that RND can serve as a supplementary tool for conventional  
314 photochemical models.

315

## 316 **5. Acknowledgements**

317

318 This study was financially supported by the National Research Foundation of Republic of  
319 Korea (2020R1A2C3014592).

320

## 321 **6. Code availability**

322

323       The RND model codes (.h5 files) with preprocessed sample data can be downloaded from  
324 (Gil, 2021).

325

## 326       **7. Author contributions**

327

328       JG and ML designed the manuscript and developed the model code. JK, GL, and JA  
329 provided the measurement data and validated the model. All the authors contributed to the  
330 manuscript.

331

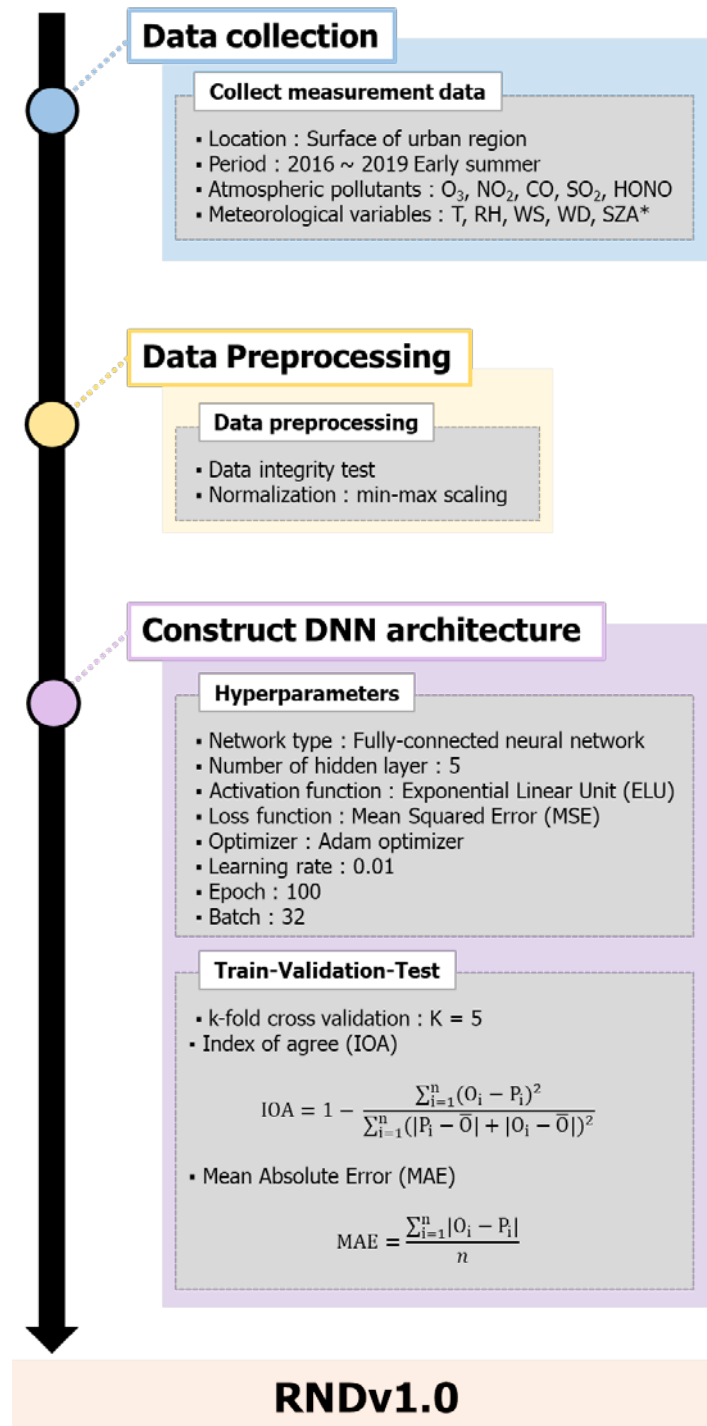
## 332       **8. Competing interests**

333

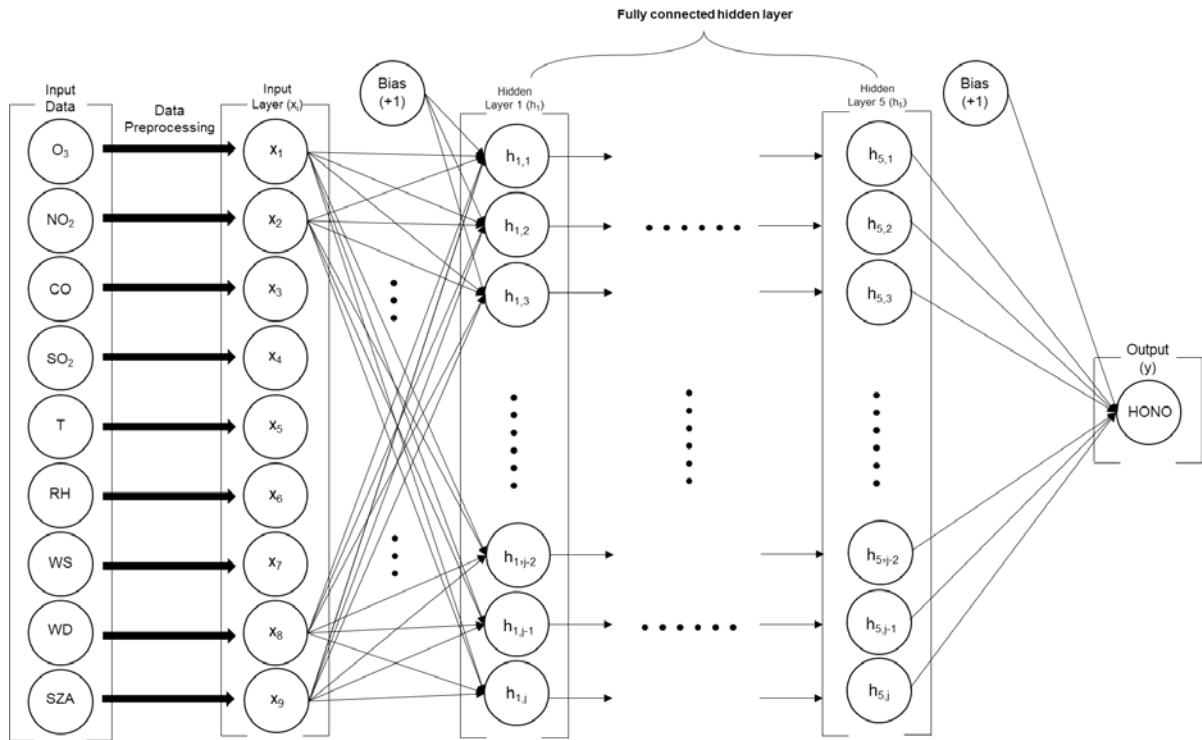
334       The authors declare that they have no conflict of interest.

335

336



340 **Figure 1.** The main processes for configuring the RNDv1.0 (\*: calculated values)

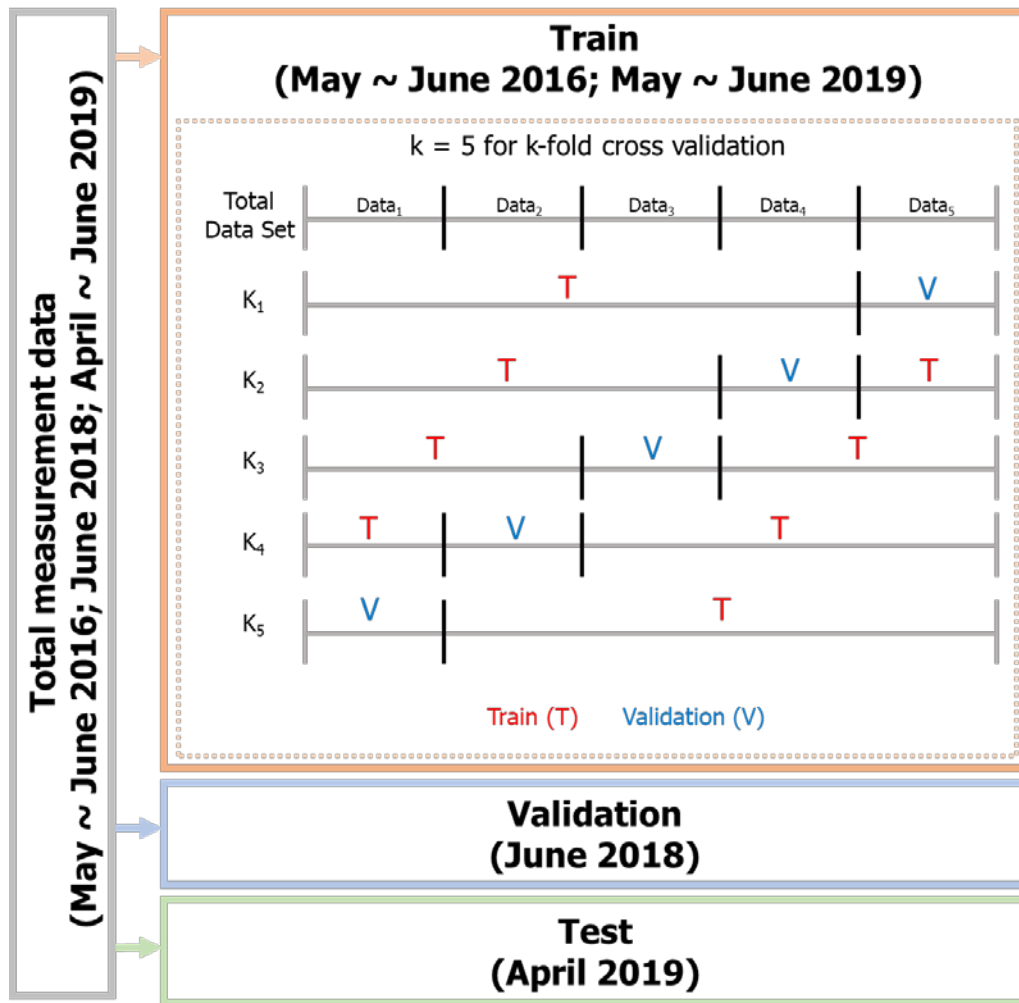


341

342 **Figure 2.** The structure of deep neural network built for RND v1.0.

343

344



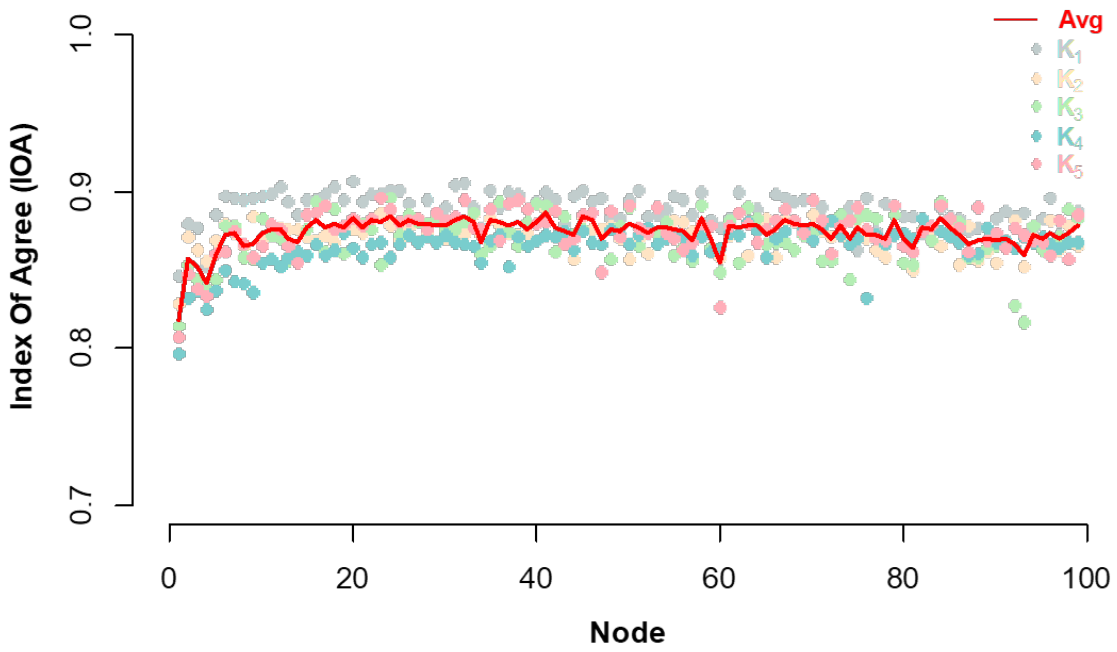
345

346 **Figure 3.** Design of training, validation, and test to build RNDv1.0 using measurement data.

347 **The k-fold cross validation were performed using randomly divided five subsets of**

348 **training data set.**

349

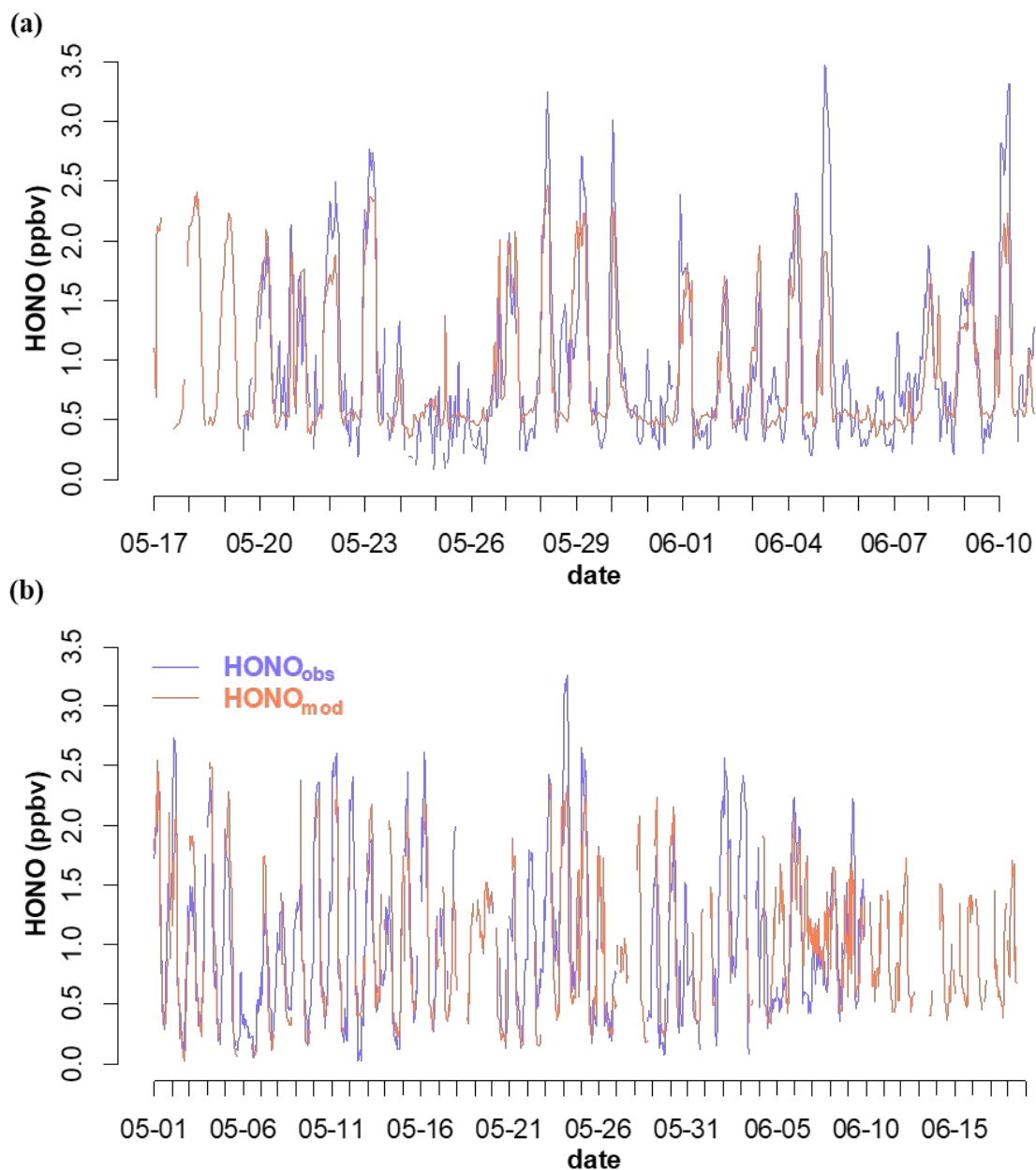


350

351 **Figure 4.** Index Of Agreement (IOA) for k-fold cross validation. Solid circle and red line  
 352 represent IOA for each validation (k=5) and the average of 5 validation sets at each node number.

353

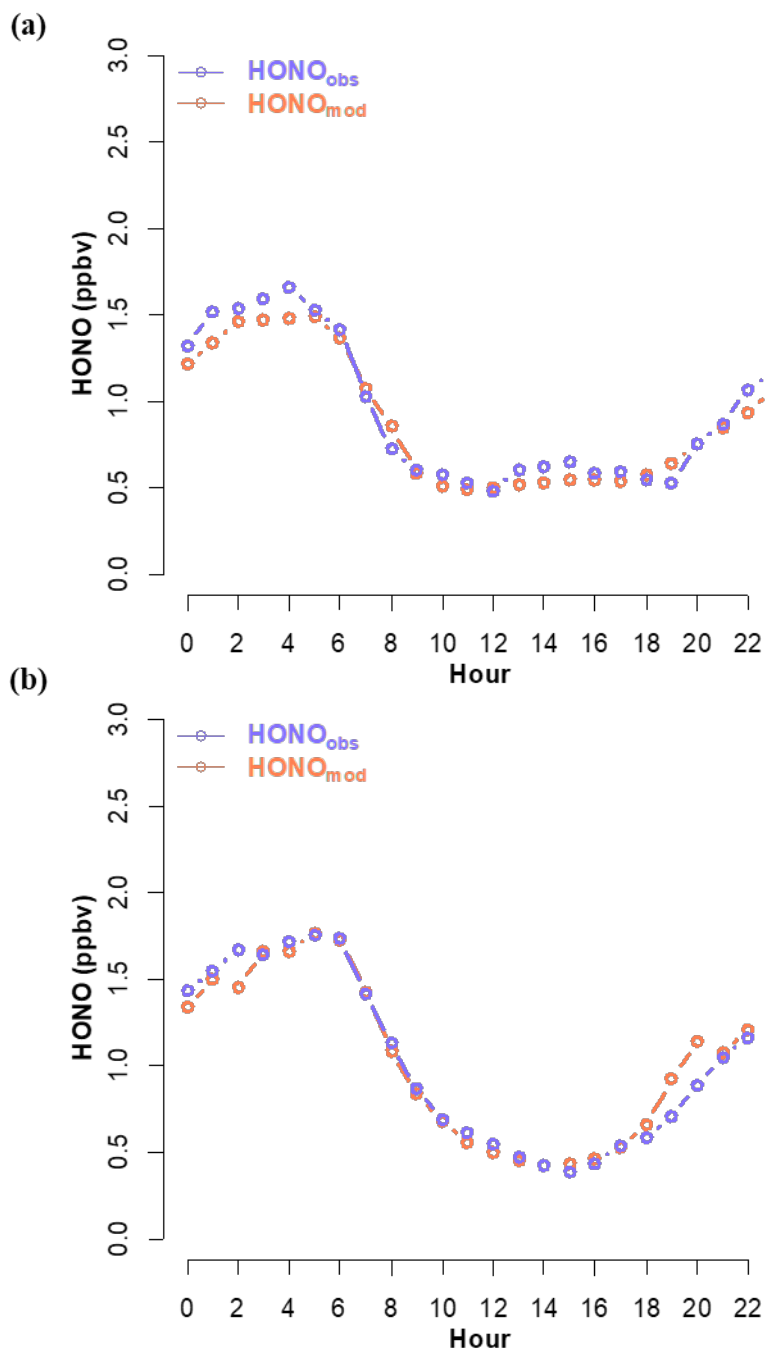




354

355 **Figure 5.** Comparison between the measured (HONO<sub>obs</sub>) and calculated (HONO<sub>mod</sub>) HONO  
 356 mixing ratios in Seoul during May~June in (a) 2016 and (b) 2019. The blue and red lines  
 357 indicate the measured and calculated HONO mixing ratio, respectively.

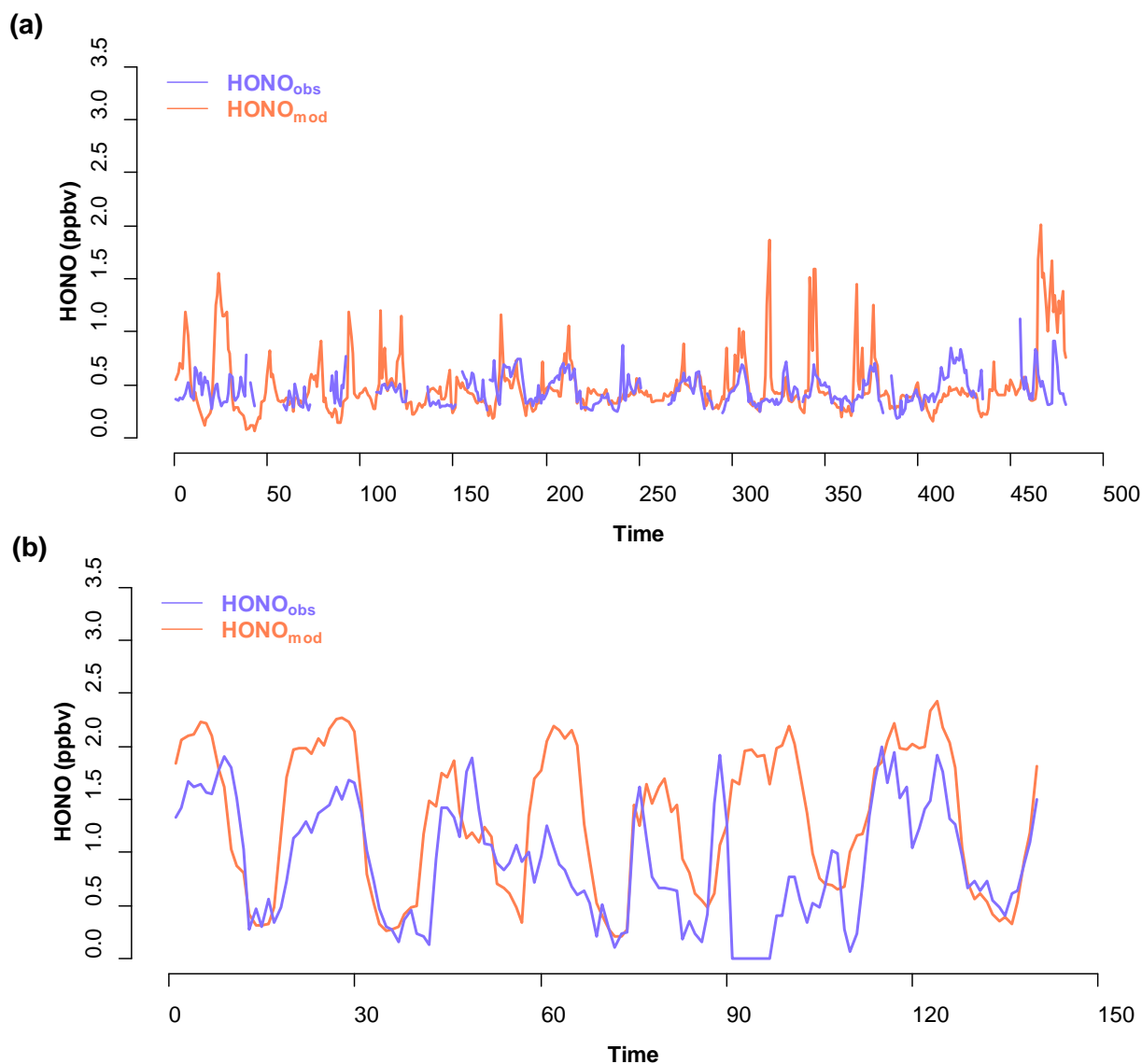
358



359

360 **Figure 6.** Average diurnal variations of the measured (HONO<sub>obs</sub>) and the calculated (HONO<sub>mod</sub>)  
 361 HONO mixing ratios in Seoul during May ~ June in (a) 2016 and (b) 2019.

362

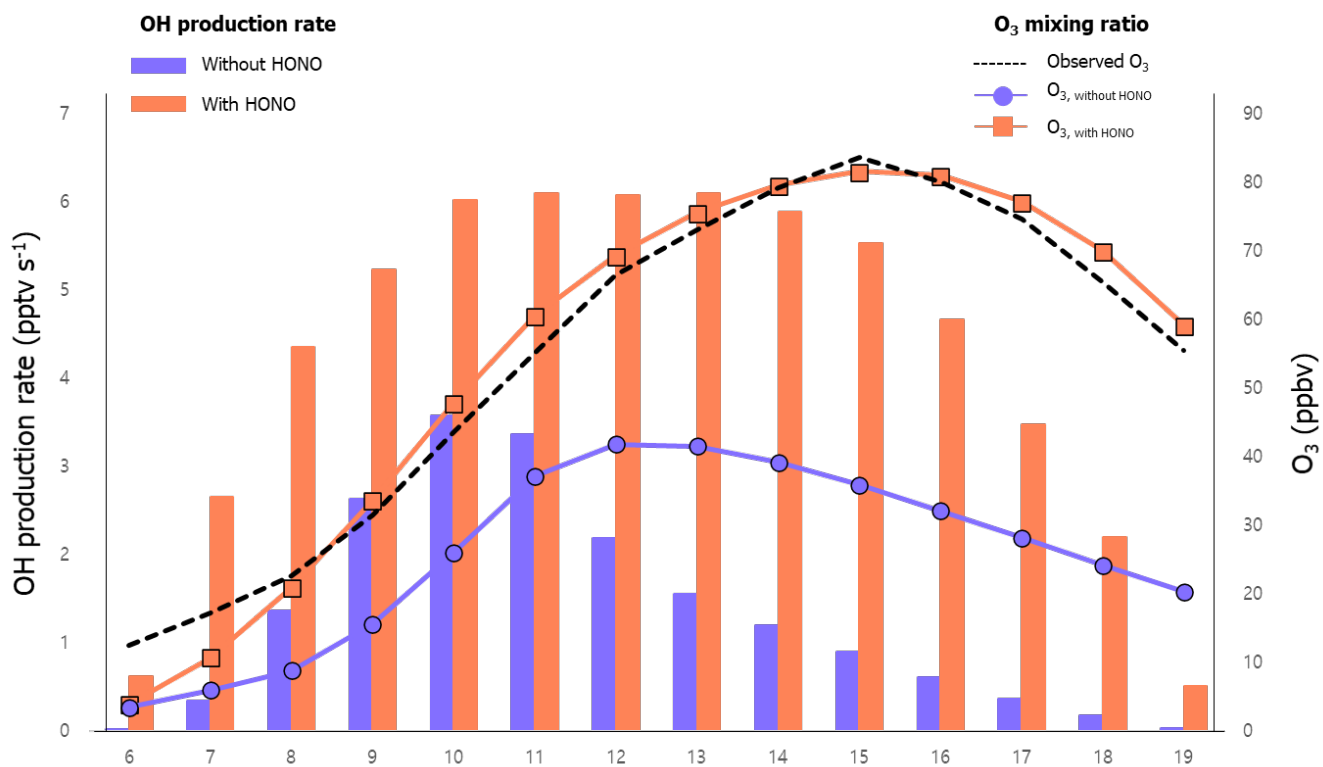


363

364 **Figure 7.** Comparison between the measured ( $\text{HONO}_{\text{obs}}$ ) and calculated ( $\text{HONO}_{\text{mod}}$ ) HONO  
 365 mixing ratios in Seoul during (a) June 2018 and (b) April 2019. The blue and red lines indicate  
 366 the measured and calculated HONO mixing ratio, respectively. The x axis indicates the hour  
 367 from the beginning of the experiment, which is (a) 00:00 on 1<sup>st</sup> June 2018 and (b) 00:00 on 12<sup>th</sup>  
 368 April 2019.

369

370



371

372 **Figure 8.** For June 2016, diurnal variations of O<sub>3</sub> (line) and OH production rate (bar) calculated  
 373 from the F0AM photochemical model with (orange) and without (blue) HONO estimated from  
 374 the RNDv1.0 model. The measured O<sub>3</sub> is compared with the calculated.

375

376 **Table 1.** Resources for constructing RND model.

	Version	Remark
Python	v3.8.3	
CUDA	v10.1	*If using GPU
CuDNN	v7.6.5	*If using GPU
Tensorflow	v2.3.0	<i>Python library</i>
Keras	v2.4.3	<i>Python library</i>
Pandas	v1.0.5	<i>Python library</i>
Numpy	v1.18.5	<i>Python library</i>

377 \*GPU denotes graphic processing unit

378 **Table 2.** Input variables of the RNDv1.0 model and their ranges (10<sup>th</sup> and 90<sup>th</sup> percentile)  
 379 observed in Seoul during May ~ June in 2016 and 2019.

	10 <sup>th</sup> ~90 <sup>th</sup> percentile (unit)	Coverage (%)	Scale Factor1 (F <sub>1</sub> )*	Scale Factor 2 (F <sub>2</sub> )**
<b>Input Variables</b>				
O <sub>3</sub>	12.1 ~ 90.4 (ppbv)	95.5	204.738	0.842
NO <sub>2</sub>	11.0 ~ 48.6 (ppbv)	80.6	79.925	2.375
CO	252 ~ 743 (ppbv)	95.1	975.248	137.253
SO <sub>2</sub>	1.9 ~ 6.4 (ppbv)	95.6	12.479	0.958
Solar Zenith Angle	22.7 ~ 118.4 (°)	100.0	112.317	14.195
Temperature	15.9 ~ 26.7 (°C)	99.4	24.240	8.610
Relative Humidity	29.2 ~ 79.1 (%)	99.4	88.545	10.555
Wind Speed	0.2 ~ 3.7 (m/s)	99.4	7.581	0.005
Wind Direction	45.4 ~ 287.5 (°)	99.4	359.565	0.235
<b>Output Variables</b>				
HONO	0.3 ~ 2.0 (ppbv)	81.1%	3.447	0.013

380 \* Maximum – Minimum

381 \*\* Minimum value

382

383 **Table 3.** The result of validation and test of RNDv1.0 model using measurement data.

Measurement data	Validation		Test	
	MAE (ppbv)	IOA	MAE (ppbv)	IOA
May 2016*	0.26	0.93		
June 2016*	0.29	0.86		
June 2018	0.21	0.79		
April 2019			0.56	0.65
May 2019*	0.26	0.93		
June 2019*	0.36	0.76		

384 \*Re-using the data already used for training

385

386 **Reference**

387

388 Akimoto, H., Nagashima, T., Li, J., Fu, J. S., Ji, D., Tan, J., and Wang, Z.: Comparison of surface  
389 ozone simulation among selected regional models in MICS-Asia III—effects of chemistry and  
390 vertical transport for the causes of difference, *Atmospheric Chemistry and Physics*, 19, 603-  
391 615, 2019.

392 Akimoto, H., and Tanimoto, H.: Review of Comprehensive Measurements of Speciated NOy  
393 and its Chemistry: Need for Quantifying the Role of Heterogeneous Processes of HNO<sub>3</sub> and  
394 HONO, *Aerosol and Air Quality Research*, 21, 200395, 2021.

395 Anderson, D. C., Loughner, C. P., Diskin, G., Weinheimer, A., Canty, T. P., Salawitch, R. J.,  
396 Worden, H. M., Fried, A., Mikoviny, T., and Wisthaler, A.: Measured and modeled CO and NOy  
397 in DISCOVER-AQ: An evaluation of emissions and chemistry over the eastern US,  
398 *Atmospheric Environment*, 96, 78-87, 2014.

399 Arcomano, T., Szunyogh, I., Wikner, A., Pathak, J., Hunt, B. R., and Ott, E.: A Hybrid Approach  
400 to Atmospheric Modeling that Combines Machine Learning with a Physics-Based Numerical  
401 Model, *Journal of Advances in Modeling Earth Systems*, e2021MS002712, 2021.

402 Arnell, N. W., Lowe, J. A., Challinor, A. J., and Osborn, T. J.: Global and regional impacts of  
403 climate change at different levels of global temperature increase, *Climatic Change*, 155, 377-  
404 391, 2019.

405 Baek, W.-K., and Jung, H.-S.: Performance Comparison of Oil Spill and Ship Classification  
406 from X-Band Dual-and Single-Polarized SAR Image Using Support Vector Machine, Random  
407 Forest, and Deep Neural Network, *Remote Sensing*, 13, 3203, 2021.

408 Bao, F., Cheng, Y., Kuhn, U., Li, G., Wang, W., Kratz, A. M., Weber, J., Weber, B., Pöschl, U.,  
409 and Su, H.: Key Role of Equilibrium HONO Concentration over Soil in Quantifying Soil–  
410 Atmosphere HONO Fluxes, *Environmental science & technology*, 2022.

411 Bengio, Y., and Grandvalet, Y.: No unbiased estimator of the variance of K-fold cross-validation,  
412 *Citeseer*, 2003.

413 Bloss, W. J., Kramer, L., Crilley, L. R., Vu, T., Harrison, R. M., Shi, Z., Lee, J. D., Squires, F.  
414 A., Whalley, L. K., and Slater, E.: Insights into air pollution chemistry and sulphate formation  
415 from nitrous acid (HONO) measurements during haze events in Beijing, *Faraday Discussions*,  
416 226, 223-238, 2021.

417 Brown, S. S., An, H., Lee, M., Park, J.-H., Lee, S.-D., Fibiger, D. L., McDuffie, E. E., Dubé,  
418 W. P., Wagner, N. L., and Min, K.-E.: Cavity enhanced spectroscopy for measurement of  
419 nitrogen oxides in the Anthropocene: results from the Seoul tower during MAPS 2015, *Faraday*  
420 *discussions*, 200, 529-557, 2017.

421 Canty, T., Hembeck, L., Vinciguerra, T., Anderson, D., Goldberg, D., Carpenter, S., Allen, D.,  
422 Loughner, C., Salawitch, R., and Dickerson, R.: Ozone and NO<sub>x</sub> chemistry in the eastern US:  
423 evaluation of CMAQ/CB05 with satellite (OMI) data, *Atmospheric Chemistry and Physics*, 15,  
424 10965-10982, 2015.

425 Chen, G., Li, S., Knibbs, L. D., Hamm, N. A., Cao, W., Li, T., Guo, J., Ren, H., Abramson, M.  
426 J., and Guo, Y.: A machine learning method to estimate PM<sub>2.5</sub> concentrations across China  
427 with remote sensing, meteorological and land use information, *Science of the Total*  
428 *Environment*, 636, 52-60, 2018a.

429 Chen, Y., Wolke, R., Ran, L., Birmili, W., Spindler, G., Schröder, W., Su, H., Cheng, Y., Tegen,  
430 I., and Wiedensohler, A.: A parameterization of the heterogeneous hydrolysis of N<sub>2</sub>O<sub>5</sub> for mass-



431 based aerosol models: improvement of particulate nitrate prediction, *Atmos. Chem. Phys.*, 18,  
432 673-689, 2018b.

433 Cheng, P., Pour-Biazar, A., White, A. T., and McNider, R. T.: Improvement of summertime  
434 surface ozone prediction by assimilating Geostationary Operational Environmental Satellite  
435 cloud observations, *Atmospheric Environment*, 268, 118751, 2022.

436 Cui, L., and Wang, S.: Mapping the daily nitrous acid (HONO) concentrations across China  
437 during 2006-2017 through ensemble machine-learning algorithm, *Science of The Total  
438 Environment*, 147325, 2021.

439 Dang, C., Liu, Y., Yue, H., Qian, J., and Zhu, R.: Autumn crop yield prediction using data-driven  
440 approaches:-support vector machines, random forest, and deep neural network methods,  
441 *Canadian Journal of Remote Sensing*, 47, 162-181, 2021.

442 Ding, B., Qian, H., and Zhou, J.: Activation functions and their characteristics in deep neural  
443 networks, 2018 Chinese control and decision conference (CCDC), 2018, 1836-1841.

444 Ge, B., Xu, X., Ma, Z., Pan, X., Wang, Z., Lin, W., Ouyang, B., Xu, D., Lee, J., and Zheng, M.:  
445 Role of Ammonia on the Feedback Between AWC and Inorganic Aerosol Formation During  
446 Heavy Pollution in the North China Plain, *Earth and Space Science*, 6, 1675-1693, 2019.

447 Gen, M., Liang, Z., Zhang, R., Mabato, B. R. G., and Chan, C. K.: Particulate nitrate photolysis  
448 in the atmosphere, *Environmental Science: Atmospheres*, 2022.

449 Gil, J., Son, J., Kang, S., Park, J., Lee, M., Jeon, E., and Shim, M.: HONO measurement in  
450 Seoul during Summer 2018 and its Impact on Photochemistry, *Journal of Korean Society for  
451 Atmospheric Environment*, 36, 579-588, 10.5572/KOSAE.2020.36.5.579, 2020.

452 Gil, J.: RNDv1.0 and example, <https://doi.org/10.5281/zenodo.5540180>, in, Zenodo, 2021.

453 Gil, J., Kim, J., Lee, M., Lee, G., Ahn, J., Lee, D. S., Jung, J., Cho, S., Whitehill, A., Szykman,  
454 J., and Lee, J.: Characteristics of HONO and its impact on O<sub>3</sub> formation in the Seoul  
455 Metropolitan Area during the Korea-US Air Quality study, *Atmospheric Environment*, 2021,  
456 <https://doi.org/10.1016/j.atmosenv.2020.118182>., 2021.

457 Gu, R., Wang, W., Peng, X., Xia, M., Zhao, M., Zhang, Y., Liu, Y., Shen, H., Xue, L., and Wang,  
458 T.: Nitrous acid in the polluted coastal atmosphere of the South China Sea: Ship emissions,  
459 budgets, and impacts, *Science of The Total Environment*, 153692, 2022.

460 IPCC: Summary for policymakers. In: *Climate Change 2014: Impacts, Adaption, and  
461 Vulnerability. Part A: Global and Sectoral Aspects. Contribution of Working Group II to the  
462 Fifth Assessment Report of the Intergovernmental Panel on Climate Change* [Field, C.B., V.R.  
463 Barros, D.J. Dokken, K.J. Mach, M.D. Mastrandrea, T.E. Bilir, M. Chatterjee, K.L. Ebi, Y.O.  
464 Estrada, R.C. Genova, B. Girma, E.S. Kissel, A.N. Levy, S. MacCracken, P.R. Mastrandrea,  
465 and L.L.White (eds.)], Cambridge, United Kingdom and New York, NY, USA, 1-32, 2014.

466 Jia, C., Tong, S., Zhang, W., Zhang, X., Li, W., Wang, Z., Wang, L., Liu, Z., Hu, B., and Zhao,  
467 P.: Pollution characteristics and potential sources of nitrous acid (HONO) in early autumn 2018  
468 of Beijing, *Science of The Total Environment*, 735, 139317, 2020.

469 Jordan, C., Crawford, J. H., Beyersdorf, A. J., Eck, T. F., Halliday, H. S., Nault, B. A., Chang,  
470 L.-S., Park, J., Park, R., Lee, G., Kim, H., Ahn, J.-y., Cho, S., Shin, H. J., Lee, J. H., Jung, J.,  
471 Kim, D.-S., Lee, M., Lee, T., Whitehill, A., Szykman, J., Schueneman, M. K., Campuzano-Jost,  
472 P., Jimenez, J. L., DiGangi, J. P., Diskin, G. S., Anderson, B. E., Moore, R. H., Ziemba, L. D.,  
473 Fenn, M. A., Hair, J. W., Kuehn, R. E., Holz, R. E., Chen, G., Travis, K., Shook, M., Peterson,  
474 D. A., Lamb, K. D., and Schwarz, J. P.: Investigation of factors controlling PM<sub>2.5</sub> variability  
475 across the South Korean Peninsula during KORUS-AQ, *Elementa: Science of the  
476 Anthropocene*, in review, 2020.

477 Joutsensaari, J., Ozon, M., Nieminen, T., Mikkonen, S., Lähivaara, T., Decesari, S., Facchini,  
478 M. C., Laaksonen, A., and Lehtinen, K. E.: Identification of new particle formation events with  
479 deep learning, *Atmospheric Chemistry and Physics*, 18, 9597-9615, 2018.

480 Kang, Y., Choi, H., Im, J., Park, S., Shin, M., Song, C.-K., and Kim, S.: Estimation of surface-  
481 level NO<sub>2</sub> and O<sub>3</sub> concentrations using TROPOMI data and machine learning over East Asia,  
482 *Environmental Pollution*, 288, 117711, 2021.

483 Kim, H., Gil, J., Lee, M., Jung, J., Whitehill, A., Szykman, J., Lee, G., Kim, D., Cho, S., Ahn,  
484 J., Hong, J., and Park, M.: Overview and characteristics of air quality in the Seoul Metropolitan  
485 Area during the KORUS-AQ campaign, *Elementa: Science of the Anthropocene*, in review,  
486 2020.

487 Kleffmann, J., Lörzer, J., Wiesen, P., Kern, C., Trick, S., Volkamer, R., Rodenas, M., and Wirtz,  
488 K.: Intercomparison of the DOAS and LOPAP techniques for the detection of nitrous acid  
489 (HONO), *Atmospheric Environment*, 40, 3640-3652, 2006.

490 Kleinert, F., Leufen, L. H., and Schultz, M. G.: IntelliO<sub>3</sub>-ts v1. 0: a neural network approach to  
491 predict near-surface ozone concentrations in Germany, *Geoscientific Model Development*, 14,  
492 1-25, 2021.

493 Krishnamurthy, R., Newsom, R. K., Berg, L. K., Xiao, H., Ma, P.-L., and Turner, D. D.: On the  
494 estimation of boundary layer heights: a machine learning approach, *Atmospheric Measurement  
495 Techniques*, 14, 4403-4424, 2021.

496 Lee, B. H., Wood, E. C., Zahniser, M. S., McManus, J. B., Nelson, D. D., Herndon, S. C.,  
497 Santoni, G., Wofsy, S. C., and Munger, J. W.: Simultaneous measurements of atmospheric  
498 HONO and NO<sub>2</sub> via absorption spectroscopy using tunable mid-infrared continuous-wave  
499 quantum cascade lasers, *Applied Physics B*, 102, 417-423, 2011.

500 Levy, M., Zhang, R., Zheng, J., Zhang, A. L., Xu, W., Gomez-Hernandez, M., Wang, Y., and  
501 Olaguer, E.: Measurements of nitrous acid (HONO) using ion drift-chemical ionization mass  
502 spectrometry during the 2009 SHARP field campaign, *Atmospheric Environment*, 94, 231-240,  
503 2014.

504 Li, S., Song, W., Zhan, H., Zhang, Y., Zhang, X., Li, W., Tong, S., Pei, C., Wang, Y., and Chen,  
505 Y.: Contribution of Vehicle Emission and NO<sub>2</sub> Surface Conversion to Nitrous Acid (HONO) in  
506 Urban Environments: Implications from Tests in a Tunnel, *Environmental Science &  
507 Technology*, 55, 15616-15624, 2021a.

508 Li, Y., Wang, X., Wu, Z., Li, L., Wang, C., Li, H., Zhang, X., Zhang, Y., Li, J., and Gao, R.:  
509 Atmospheric nitrous acid (HONO) in an alternate process of haze pollution and ozone pollution  
510 in urban Beijing in summertime: Variations, sources and contribution to atmospheric  
511 photochemistry, *Atmospheric Research*, 260, 105689, 2021b.

512 Li, Z., Xie, P., Hu, R., Wang, D., Jin, H., Chen, H., Lin, C., and Liu, W.: Observations of N<sub>2</sub>O<sub>5</sub>  
513 and NO<sub>3</sub> at a suburban environment in Yangtze river delta in China: Estimating heterogeneous  
514 N<sub>2</sub>O<sub>5</sub> uptake coefficients, *Journal of Environmental Sciences*, 2020.

515 Liebmann, J., Karu, E., Sobanski, N., Schuladen, J., Ehn, M., Schallhart, S., Quéléver, L.,  
516 Hellen, H., Hakola, H., and Hoffmann, T.: Direct measurement of NO<sub>3</sub> radical reactivity in a  
517 boreal forest, *Atmospheric Chemistry and Physics*, 2018.

518 Liu, Y., Lu, K., Li, X., Dong, H., Tan, Z., Wang, H., Zou, Q., Wu, Y., Zeng, L., and Hu, M.: A  
519 comprehensive model test of the HONO sources constrained to field measurements at rural  
520 North China Plain, *Environmental science & technology*, 53, 3517-3525, 2019.

521 Mallet, V., and Sportisse, B.: Uncertainty in a chemistry-transport model due to physical  
522 parameterizations and numerical approximations: An ensemble approach applied to ozone  
523 modeling, *Journal of Geophysical Research: Atmospheres*, 111, 2006.

524 Meng, F., Qin, M., Fang, W., Duan, J., Tang, K., Zhang, H., Shao, D., Liao, Z., Feng, Y., and  
525 Huang, Y.: Measurement of HONO flux using the aerodynamic gradient method over an  
526 agricultural field in the Huaihe River Basin, China, *Journal of Environmental Sciences*, 2022.

527 Monks, P. S., Archibald, A., Colette, A., Cooper, O., Coyle, M., Derwent, R., Fowler, D.,  
528 Granier, C., Law, K. S., and Mills, G.: Tropospheric ozone and its precursors from the urban to  
529 the global scale from air quality to short-lived climate forcer, *Atmospheric Chemistry and*  
530 *Physics*, 15, 8889-8973, 2015.

531 Myhre, G., Aas, W., Cherian, R., Collins, W., Faluvegi, G., Flanner, M., Forster, P., Hodnebrog,  
532 Ø., Klimont, Z., and Lund, M. T.: Multi-model simulations of aerosol and ozone radiative  
533 forcing due to anthropogenic emission changes during the period 1990–2015, *Atmospheric*  
534 *Chemistry and Physics*, 17, 2709-2720, 2017.

535 Peterson, D. A., Hyer, E. J., Han, S.-O., Crawford, J. H., Park, R. J., Holz, R., Kuehn, R. E.,  
536 Eloranta, E., Knute, C., and Jordan, C. E.: Meteorology influencing springtime air quality,  
537 pollution transport, and visibility in Korea, *Elem Sci Anth*, 7, 2019.

538 Pinto, J., Dibb, J., Lee, B., Rappenglück, B., Wood, E., Levy, M., Zhang, R. Y., Lefer, B., Ren,  
539 X. R., and Stutz, J.: Intercomparison of field measurements of nitrous acid (HONO) during the  
540 SHARP campaign, *Journal of Geophysical Research: Atmospheres*, 119, 5583-5601, 2014.

541 Reichstein, M., Camps-Valls, G., Stevens, B., Jung, M., Denzler, J., and Carvalhais, N.: Deep  
542 learning and process understanding for data-driven Earth system science, *Nature*, 566, 195-204,  
543 2019.

544 Roberts, J. M., Veres, P., Warneke, C., Neuman, J., Washenfelder, R., Brown, S., Baasandorj,  
545 M., Burkholder, J., Burling, I., and Johnson, T. J.: Measurement of HONO, HNCO, and other  
546 inorganic acids by negative-ion proton-transfer chemical-ionization mass spectrometry (NI-PT-  
547 CIMS): Application to biomass burning emissions, *Atmospheric Measurement Techniques*, 3,  
548 981, 2010.

549 Schultz, M., Betancourt, C., Gong, B., Kleinert, F., Langguth, M., Leufen, L., Mozaffari, A.,  
550 and Stadtler, S.: Can deep learning beat numerical weather prediction?, *Philosophical*  
551 *Transactions of the Royal Society A*, 379, 20200097, 2021.

552 Shahriar, S. A., Kayes, I., Hasan, K., Salam, M. A., and Chowdhury, S.: Applicability of  
553 machine learning in modeling of atmospheric particle pollution in Bangladesh, *Air Quality,*  
554 *Atmosphere & Health*, 13, 1247-1256, 2020.

555 Shareef, M. M., Husain, T., and Alharbi, B.: Studying the Effect of Different Gas-Phase  
556 Chemical Kinetic Mechanisms on the Formation of Oxidants, Nitrogen Compounds and Ozone  
557 in Arid Regions, *Journal of Environmental Protection*, 10, 1006-1031, 2019.

558 Shindell, D. T., Lamarque, J.-F., Schulz, M., Flanner, M., Jiao, C., Chin, M., Young, P., Lee, Y.  
559 H., Rotstayn, L., and Mahowald, N.: Radiative forcing in the ACCMIP historical and future  
560 climate simulations, *Atmospheric Chemistry and Physics*, 13, 2939-2974, 2013.

561 Stadtler, S., Simpson, D., Schröder, S., Taraborrelli, D., Bott, A., and Schultz, M.: Ozone  
562 impacts of gas–aerosol uptake in global chemistry transport models, *Atmospheric chemistry*  
563 *and physics*, 18, 3147-3171, 2018.

564 Stevenson, D., Young, P., Naik, V., Lamarque, J.-F., Shindell, D. T., Voulgarakis, A., Skeie, R.  
565 B., Dalsoren, S. B., Myhre, G., and Berntsen, T. K.: Tropospheric ozone changes, radiative  
566 forcing and attribution to emissions in the Atmospheric Chemistry and Climate Model  
567 Intercomparison Project (ACCMIP), *Atmospheric Chemistry and Physics*, 13, 3063-3085, 2013.

568 Sumathi, S., and Pugalendhi, G. K.: Cognition based spam mail text analysis using combined  
569 approach of deep neural network classifier and random forest, *Journal of Ambient Intelligence*  
570 *and Humanized Computing*, 12, 5721-5731, 2021.

571 Sun, Y., Wang, L., Wang, Y., Quan, L., and Zirui, L.: In situ measurements of SO<sub>2</sub>, NO<sub>x</sub>, NO<sub>y</sub>,  
572 and O<sub>3</sub> in Beijing, China during August 2008, *Science of the Total Environment*, 409, 933-940,  
573 2011.

574 Tie, X., Geng, F., Guenther, A., Cao, J., Greenberg, J., Zhang, R., Apel, E., Li, G., Weinheimer,  
575 A., and Chen, J.: Megacity impacts on regional ozone formation: observations and WRF-Chem  
576 modeling for the MIRAGE-Shanghai field campaign, *Atmospheric Chemistry and Physics*, 13,  
577 5655-5669, 2013.

578 VandenBoer, T., Markovic, M., Sanders, J., Ren, X., Pusede, S., Browne, E., Cohen, R., Zhang,  
579 L., Thomas, J., and Brune, W. H.: Evidence for a nitrous acid (HONO) reservoir at the ground  
580 surface in Bakersfield, CA, during CalNex 2010, *Journal of Geophysical Research:*  
581 *Atmospheres*, 119, 9093-9106, 2014.

582 Varotsos, K., Giannakopoulos, C., and Tombrou, M.: Assessment of the Impacts of climate  
583 change on european ozone levels, *Water, Air, & Soil Pollution*, 224, 1-13, 2013.

584 Wang, H., Chen, X., Lu, K., Hu, R., Li, Z., Wang, H., Ma, X., Yang, X., Chen, S., and Dong,  
585 H.: NO<sub>3</sub> and N<sub>2</sub>O<sub>5</sub> chemistry at a suburban site during the EXPLORE-YRD campaign in 2018,  
586 *Atmospheric Environment*, 224, 117180, 2020.

587 Wang, T., Qin, Z., and Zhu, M.: An ELU network with total variation for image denoising,  
588 *International Conference on Neural Information Processing*, 2017a, 227-237.

589 Wang, X., Wang, H., Xue, L., Wang, T., Wang, L., Gu, R., Wang, W., Tham, Y. J., Wang, Z.,  
590 and Yang, L.: Observations of N<sub>2</sub>O<sub>5</sub> and ClNO<sub>2</sub> at a polluted urban surface site in North China:  
591 High N<sub>2</sub>O<sub>5</sub> uptake coefficients and low ClNO<sub>2</sub> product yields, *Atmospheric environment*, 156,  
592 125-134, 2017b.

593 Wolfe, G. M., Marvin, M. R., Roberts, S. J., Travis, K. R., and Liao, J.: The framework for 0-  
594 D atmospheric modeling (F0AM) v3. 1, *Geoscientific Model Development*, 9, 3309, 2016.

595 Xu, Z., Liu, Y., Nie, W., Sun, P., Chi, X., and Ding, A.: Evaluating the measurement interference  
596 of wet rotating-denuder-ion chromatography in measuring atmospheric HONO in a highly  
597 polluted area, *Atmospheric Measurement Techniques*, 12, 6737-6748, 2019.

598 Xue, C., Ye, C., Ma, Z., Liu, P., Zhang, Y., Zhang, C., Tang, K., Zhang, W., Zhao, X., and Wang,  
599 Y.: Development of stripping coil-ion chromatograph method and intercomparison with CEAS  
600 and LOPAP to measure atmospheric HONO, *Science of The Total Environment*, 646, 187-195,  
601 2019.

602 Ye, C., Zhou, X., Pu, D., Stutz, J., Festa, J., Spolaor, M., Tsai, C., Cantrell, C., Mauldin, R. L.,  
603 and Campos, T.: Rapid cycling of reactive nitrogen in the marine boundary layer, *Nature*, 532,  
604 489-491, 2016.

605